Nature Communications

https://doi.org/10.1038/s41467-026-71055-1

Article in Press

Multi-field coupling enhanced plasmonic $Mo^{\delta+}$ active site to efficiently hydrolyze ammonia borane

Received: 7 November 2025

Accepted: 12 March 2026

Cite this article as: Li, P., Tu, N., Yang, Y. *et al.* Multi-field coupling enhanced plasmonic $Mo^{\delta+}$ active site to efficiently hydrolyze ammonia borane. *Nat Commun* (2026). https://doi.org/10.1038/s41467-026-71055-1

Pengcheng Li, Nengrong Tu, Yang Yang, Junxiang Li, Huilin Hou, Dongjiang Yang & Weiyou Yang

Multi-field Coupling Enhanced Plasmonic $Mo^{\delta+}$ Active Site to Efficiently Hydrolyze Ammonia Borane

Pengcheng Li[1,ζ], Nengrong Tu[1,ζ], Yang Yang[1,*], Junxiang Li[1], Huilin Hou[1], Dongjiang Yang[1,*] and Weiyou Yang[1,*]

[1]Institute of Micro/Nano Materials and Devices, Ningbo University of Technology, Ningbo City, 315211, P. R. China

[ζ]Contribute equally to this work

[*]Corresponding Authors Emails: yangyangafterglow@yeah.net; d.yang@qdu.edu.cn; weiyouyang@tsinghua.org.cn

Rapid recombination of photogenerated carriers and weak driving forces to inject hot electrons are critical bottlenecks in solar-driven ammonia borane hydrolysis. Herein, aided by machine learning, plasmon polarization-induced multi-field coupling is developed to enhance ammonia borane hydrolytic activity. The reconstructed surface unsaturated $Mo^{\delta+}$ active sites exhibit well activity and high stability over 100 hours in AB hydrolysis, which deliver a turnover frequency up to 5806 min^{-1}, representing competitiveness compared to non-noble and noble-metal based catalysts ever reported. It is verified that the polarized electric field facilitates carrier separation through incorporating polarization components (O_v and -OH), thereby promoting electron accumulation around $Mo^{\delta+}$ active sites. Meanwhile, the local electric field enables highly delocalized hot electrons through plasmon oscillation, thus lowering the reaction barrier between $Mo^{\delta+}$ and AB. In this work, the hot electrons are efficiently channeled via an enhanced feedback pathway, facilitating their transfer into B-H antibonding orbitals toward boosted AB hydrolysis.

Solar-driven hydrogen production is considered the most promising and environmentally friend approach to producing hydrogen fuel[1-5]. Particularly, the photocatalytic hydrolysis of Ammonia borane (NH_3BH_3, AB) has received extensive attention[6-10], since the outstanding gravimetric hydrogen storage capacity of AB (19.6 wt%) exceeds that of conventional hydrogen storage materials. In addition, different with gaseous hydrogen storage systems, AB offers distinct

advantages in terms of liquid-phase storage and transportation, combining high fluidity with low vapor pressure, thereby mitigating safety risks associated with compressed hydrogen. Generally, the hydrolysis reaction of AB can be precisely regulated via catalysts to achieve efficient, green, and clean hydrogen release[11-14]. A perfect photocatalytic material for AB hydrolysis would not only have efficient light absorption and charge separation, but also possess surface unsaturated metal ($M^{\delta+}$, such as $Pt^{\delta+}$, $Ru^{\delta+}$) sites to trigger the hydrolysis of AB[15-20]. Generally, $M^{\delta+}$ active site with unfilled *d*-electron orbitals forms M-$BH_2^+NH_3$ complex with AB through the M-B bond, because the N atom in AB supplies its lone pair electrons to the empty orbital of the B atom. Then the *d*-electrons of $M^{\delta+}$ active site feedback to the anti-bonding orbitals of AB, and thus weaken and elongate the B-H bond. Apparently, the designed photocatalyst requires that the unsaturated $M^{\delta+}$ active sites have an empty orbital to accept the electrons of AB, effectively capturing and activating the reaction molecule AB. Additionally, a driving force in designed photocatalyst is essential to separate the charges in the bulk or on the surface and feeding them the antibonding orbitals of AB.

Plasmonic photocatalysts, loaded with noble metal or transition metal nanoparticles (Au, Al, Cu, etc.) on semiconductor substrates, offer powerful surface plasmon resonance (SPR) to enhance the photocatalytic activity[21,22]. More importantly, the plasmonic nanoparticles have the great potential to act as $M^{\delta+}$ active site for AB absorption and hydrolysis due to the fact that the *d*-band center of plasmonic $M^{\delta+}$ active site is close to the Fermi level, as well as the high concentration and high delocalized photo-generated carriers and d electrons near plasmonic $M^{\delta+}$[23-25]. Particularly, heavily doped semiconductor MoO_{3-x} with the plasmonic properties have attracted great attention, because it possesses wide absorption capacity ranging from ultraviolet to near-infrared (UV-

NIR)[26,27]. The exposed high oxidation state $Mo^{\delta+}$ active sites adjacent to O-vacancies exhibit a strong electron-deficient state capable of strongly adsorbing AB and possess *d*-electrons that feedback to the antibonding orbitals to promote hydrolysis. Upon photoexcitation, the collective oscillation of a large number of excess electrons near the surface $Mo^{\delta+}$ active sites induce the local electric field (LEF) resonance. This local electric field effects triggered by plasmonic nanoparticles develops a force to drive free electrons move on the surface and pump generated high-energy hot electrons to the antibonding orbitals of AB through the Mo-B bond. This near-field driving force breaks through the thermodynamic limit and realizes the spatial charge transfer between the $Mo^{\delta+}$ active sites and AB. However, the problem of electron-deficient near the $Mo^{\delta+}$ active sites and the electron-hole recombination within the catalyst occurs very rapidly (on the order of picoseconds), resulting in insufficient accessible electrons from $Mo^{\delta+}$ sites to AB. Much recently, polarization effect within a catalyst based on the construction of non-centrosymmetric structures has been proposed. The formed polarized electric field (PEF) directly drives the effective separation of photo-generated charge carriers in the bulk phase, and accelerates the direct transport and aggregation of charge carriers near $Mo^{\delta+}$ active sites[28,29]. Apparently, integrating LEF and PEF into a multi-field coupling system could firstly promote charge separation and directional extraction at the $Mo^{\delta+}$ active sites efficiently. Then, this system enables prompt injection of the high energy hot electrons into reaction molecules (AB and H_2O), achieving the dissociation of the chemical bonds (B-N, B-H bonds)[30,31].

In this study, we propose a strategy for multi-field-coupling-mediated reduction of activation barrier between the active $Mo^{\delta+}$ site and AB decomposition by reconstructing the local electronic

structure of the targeted $Mo^{\delta+}$ species. Specifically, molybdenum-oxide based heterojunctions with double plasmonic characteristics are synthesized via electrostatic self-assembly method. The plasmonic Ti_3C_2-OH in heterojunctions are also employed as excitation sources for polarization field composed of OH-O_v. Under the PEF effect, carriers are highly concentrated at the surface $Mo^{\delta+}$ sites. The delocalized hot electrons generated by LEF near $Mo^{\delta+}$ active sites pour into the anti-bonding orbitals of AB. As expected, the streamlined $Mo^{\delta+}$ active site exhibits a well catalytic activity with a high turnover frequency (TOF) of 5806 min^{-1}, outperforming most noble metals. Combining ab initio molecular dynamics (AIMD) and ligand field theory, a large number of hot electrons around $Mo^{\delta+}$ reduce the reaction potential barrier of AB hydrolysis. Here, the intermediate product ($NH_3BH_3^*$, $NH_3BH_2^*$ etc.) strongly adsorbs with H_2O, shortening the proton migration path and accelerating reaction rates. This work constructs plasmon polarization induced multi-field cooperative coupling structures to solve the low AB hydrolysis activity of molybdenum-oxide based heterojunctions, which provides a constructive idea for designing next-generation photocatalytic materials at the atomic-level.

Results

As shown in Fig. 1a, an optimal $Mo^{\delta+}$ active site is constructed to trigger the photocatalytic AB hydrolysis by providing a high concentration of delocalized hot carriers to lower the reaction barrier. To design catalysts with higher activity, machine learning (ML) algorithm is used to predict the important descriptors that affect the Gibbs free energy of AB adsorbed on $Mo^{\delta+}$ active sites. Here, a characteristic parameter p is defined based on the electronegativity difference, oxidation state, and atomic radius difference to quantify the carrier concentration for amplifying

the feature space. The Gibbs free energy of AB bound to the adsorption site is selected as the training target value. The appropriate descriptors in correlation heatmap are selected for training the model (Fig. 1b). The Fine gaussian SVM function is determined based on the R^2 result being close to 1 and the minimum root mean square error (RMSE) between the predicted values and the actual values (Fig. 1c and Supplementary Fig. 1). The results reveal that the carrier concentration p accounts for ~ 25%, which is higher than other descriptors such as metallic radius (~ 20%) and number of valence electrons (~ 17%). Obviously, the carrier concentration p seriously affects the AB hydrolysis (Fig. 1d). Based on the prediction of ML method, this study strategically adopts plasmonic MoO_{3-x} to provide 4*d* Mo active sites with high delocalization characteristics. Simultaneously, in combination with highly conductive plasmonic Ti_3C_2-OH, an O_v-OH interface polarization field is constructed in MoO_{3-x} species. This strategy thereby achieves high carrier aggregation at the $Mo^{\delta+}$ active sites which can be visually verified by the electron localization function (ELF) and the Bader charge results (Supplementary Fig. 2) based on the optimized computational models of the materials provided in Supplementary Data 1.

The adsorption dynamic process of reaction molecules (AB and H_2O) near $Mo^{\delta+}$ active site is evaluated through AIMD. The AB water solution system model of MoO_{3-x} and MoO_{3-x}/Ti_3C_2-OH are simulated dynamically, and the initial and final configurations of molecular dynamics trajectories are supplied in Supplementary Data 1. As shown in Fig. 1e, f, compared with pristine MoO_{3-x}, the adsorption $Mo^{\delta+}$ active site on the surface of MoO_{3-x}/Ti_3C_2-OH is co-regulated by steric hindrance and hydrophobic effects. The peak position (3.41 Å) of AB in MoO_{3-x}/Ti_3C_2-OH system is shorter than that in MoO_{3-x} system (3.76 Å) in Fig. 1g. This significantly promotes the

targeted adsorption of AB to the reconstructed $Mo^{\delta+}$ active site and limits the access of H_2O molecules, implying H_2O molecules are preferentially adsorbed onto AB (Supplementary Figs. 3-5). In addition, Fig. 1g reveals that the surface active sites on the MoO_{3-x}/Ti_3C_2-OH could facilitate the Jahn-Teller distortion of the adsorbed AB molecules, resulting in an obvious symmetry distortion of AB structure (85.8°-90.7°-126.5°). Obviously, the directional adsorption and structural distortion of AB stemmed from the re-constructed $Mo^{\delta+}$ active site efficiently optimize the catalytic pathway and simultaneously activate the reaction molecules (AB and H_2O), thereby achieving efficient hydrogen production.

Encouraged by the theoretical results, we prepared a heavily doped semiconductor MoO_{3-x} with unsaturated $Mo^{\delta+}$ active sites by solvothermal method, and then obtained MoO_{3-x}/Ti_3C_2-OH catalytic system through loading Ti_3C_2-OH quantum dots on the MoO_{3-x} surface via electrostatic self-assembly (Supplementary Figs. 6, 7 and Supplementary Table 1). Under the thermal cutting effect of ammonia, it is found that the -OH group can replace -F ones on the Ti_3C_2 surface through the Fourier transformed infrared (FTIR) spectra in Supplementary Fig. 8. The Zeta potential of the prepared Ti_3C_2-OH nanosheets is -7.86 mV due to the surface negatively charged -OH group (Supplementary Fig. 9). The zeta value of MoO_{3-x} shows a relatively positive potential owing to the presence of positively charged oxygen vacancies. Furthermore, the g-value of MoO_{3-x} loading Ti_3C_2-OH the show a significant reduction in the number of oxygen vacancies in the electron magnetic resonance (EPR), implying the formation of O_v-OH structure (Supplementary Fig. 10). The X-ray absorption near-edge structure (XANES) of Mo K-edge and Ti K-edge is carried out to investigate the change of coordination environment in MoO_{3-x} and MoO_{3-x}/Ti_3C_2-OH (Fig. 2a and

Supplementary Fig. 11). The absorption edge of MoO_{3-x}/Ti_3C_2-OH locates between those of MoO_2 and MoO_3, suggesting the formation of unsaturated valence states (4+/5+) of $Mo^{\delta+}$ active sites[32,33]. It is disclosed the Mo K-edge curve of MoO_{3-x}/Ti_3C_2-OH is closer to that of MoO_3 than that of MoO_{3-x}, while the Ti K-edge XANES absorption edge of MoO_{3-x}/Ti_3C_2-OH shifts toward lower energy compared with Ti_3C_2-OH. These results witness that the electron transfer from MoO_{3-x} to Ti_3C_2-OH, in consistence with the XPS results (Supplementary Figs. 12-14). As observed in the Fourier-transform (FT) extended X-ray absorption fine structure spectra and wavelet-transform (WT) profiles (Fig. 2b, c and Supplementary Fig. 15), MoO_{3-x} and MoO_{3-x}/Ti_3C_2-OH show bond length variations compared to MoO_3, and their spectral features are distinctly different from those of MoO_2. This confirms that the structural changes in MoO_{3-x}/Ti_3C_2-OH originate from O_v-induced unsaturated Mo coordination and lattice distortion, rather than a significant shift in Mo oxidation state. The positive shift of the Mo-O bond in MoO_{3-x}/Ti_3C_2-OH is relative to that of MoO_{3-x}, where the heterojunction preserves oxygen vacancies to break the original ordered six-coordinate environment and form a highly distorted coordination field, remodeling the high activity of $Mo^{\delta+}$ site. Besides, the O_v-OH structure at the MoO_{3-x}/Ti_3C_2-OH interface forms PEF, causing the Mo-O bond to be elongated due to surface electrostatic interaction. Apparently, the surface of the designed catalytic system is rich in highly active unsaturated sites, which not only aligns with the ML predictions but also provides feasibility for the subsequent effective hydrolysis of AB adsorption.

As shown in the two-dimensional differential charge density maps (Supplementary Fig. 16 and Fig. 2d), a non-centrosymmetric system composed of the oxygen defects and hydroxyl

functional groups lead to a local redistribution of charge at the MoO_{3-x}/Ti_3C_2-OH contact interface. This offers the opportunity to form an interfacial dipole layer and to generate a strong interfacial PEF. Clearly, the MoO_{3-x}/Ti_3C_2-OH heterojunction exhibits a dipole moment (4.99) that is much greater than that of the individual MoO_{3-x} (0.17) and Ti_3C_2-OH (2.31). In addition, the static potential difference value ($\Delta V \approx 1.77$ eV) of MoO_{3-x}/Ti_3C_2-OH system is much higher than that of the MoO_3/Ti_3C_2 heterojunction ($\Delta V \approx 0.7$ eV). This indicates the surface modification of structural defect (O_v) and functional groups (-OH) enhances the interfacial electric field and thus drives charge transfer and segregation from MoO_{3-x} to Ti_3C_2-OH (Fig. 2e, f and Supplementary Fig. 17)[34]. To further verify the formation of PEF through experiments, the cyclic voltammetry (CV) curves of different cathodes at a scan rate of 1mV s^{-1} are exhibited in Fig. 2g. The MoO_{3-x}/Ti_3C_2-OH (0.073 V) displays a remarkably reduced the difference of the redox potential compared with Ti_3C_2-OH (0.167 V) and MoO_{3-x} (0.115 V)[35,36]. These indicate that the interface PEF of MoO_{3-x}/Ti_3C_2-OH enhances the redox activity and accelerates the transfer rate of charge carriers on the surface. The phonon spectra and phonon density of states also indicate that the reduction of crystal symmetry increases the proportion of effective high-frequency phonons, and the enhanced polarization field accompanying the photothermal effect better drives electron migration (Supplementary Fig. 18). In-situ Kelvin probe force microscopy (KPFM) images reveal that the ultra-thin layered structure (4.6 nm) and the surface potential of MoO_{3-x}/Ti_3C_2-OH (34 mV) catalytic system is higher than MoO_{3-x} (21 mV) in Fig. 2h, i. Based on the results of zeta potential and surface potential, the interface electric field (IEF) strength of MoO_{3-x}/Ti_3C_2-OH is quantitatively determined to be 3.35 times that of the MoO_{3-x} components according to Gouy-

Chapman equation. The constructed strong interfacial PEF enhances the built-in electric field (BEF) formed by Fermi level differences to effectively separate photo-generated charge carriers in the bulk phase. This could accelerate the directional transport and aggregation of charge carriers near $Mo^{\delta+}$ active sites.

The PEF separated photo-generated electrons acquire high energy far exceeding the Fermi level and become hot electrons which are more efficiently pumped into the adsorbed AB molecules to weaken the B-H bond. Fortunately, an SPR-induced LEF can offer the photo-generated electrons near $Mo^{\delta+}$ active site high energy through the Landau damping. To clarify the SPR-generated LEF behavior under illumination, a finite element method is analyzed to simulate the LEF distribution of MoO_{3-x} and MoO_{3-x}/Ti_3C_2-OH. As shown in Fig. 3a and Supplementary Figs. 19, 20, a strong LEF coupling under 800 nm illumination occurs between Ti_3C_2-OH and MoO_{3-x}, with an enhancement factor of $|E/E_0|^2$ as high as 1154. This value is an order of magnitude higher than that of the single component. This enhanced LEF can further increase the number of delocalized hot electrons making them easier to activate AB molecule. In addition, the local temperature of the sample surface rises rapidly at the beginning of the light irradiation and stabilizes after 5 min. As demonstrated in the thermographic image in Fig. 3a, the steady-state surface temperature of MoO_{3-x}/Ti_3C_2-OH reaches 112 °C, which is higher than that of MoO_{3-x} (72 °C). This photothermal effect originates from the energy collision of excited electrons during non-radiative relaxation, which is beneficial for the transfer of hot electrons from the $Mo^{\delta+}$ active site to AB.

Surface potential measurement is employed to verify the existence of LEF-induced hot electrons in the designed catalyst under illumination. As displayed in Fig. 3b, c and Supplementary

Fig. 21, upon NIR-light irradiation, a significant enhancement in the surface photovoltage (V_s = 65 mV) of the MoO_{3-x}/Ti_3C_2-OH is observed compared to that under the dark (V_s = 34 mV). Apparently, plasmonic heterojunction system displays comparatively strong surface potential distributions under full-spectrum solar illumination (AM 1.5), with V_s value of 75 mV. This means that the hot electrons aggregation around $Mo^{\delta+}$ active sites are significantly enhanced by plasmonic LEF. The linear sweep voltammetry (LSV) curves for MoO_{3-x}/Ti_3C_2-OH at a current density of 0.1 $mA \cdot cm^{-2}$ are presented in Fig. 3d. The overpotential (η) progressively decreases from -1.14 V (in the dark) to -1.09 V under NIR light and to -1.04 V under full-spectrum light. This trend continues with cooling, further reducing the overpotential to -1.11 V (NIR light) and -1.08 V (full-spectrum light). These confirm that the PEF-induced electrons gathered at $Mo^{\delta+}$ active sites become high-energy hot electrons under the strong LEF effect.

A three-dimensional charge density difference is utilized to simulate the effect of an LEF on the distribution of the electrons in a catalytic system. As seen in Fig. 3e, a more significant accumulation of charge is detected under +0.02 eV/Å electric field, compared to the negative field and the absence of a field. This indicates that a positive LEF can optimize electronic rearrangement and accelerate the transfer of excited electrons towards the catalyst surface. The transfer kinetics of the excited hot electrons under light irradiation is revealed through transient absorption (TA) measurements. As exhibited in Fig. 3f, g and Supplementary Fig. 22, significantly enhanced ground state bleaching (GSB) signal at 494 nm are detected in the MoO_{3-x}/Ti_3C_2-OH compared with those of MoO_{3-x}. A stronger excited states absorption (ESA) signal at 511 nm in the positive absorption range is observed where the excited electrons transform into hot electrons through

electron-electron scattering and transfer to a high-energy surface plasmon (SP) state. It was found that the signal difference of excited state absorption under laser pulse (ΔA) initially increased, followed by decrease (Fig. 3g). It should be ascribed to the synergistic effect of GSB and ESA, which describes the excitation-relaxation process of excited electrons within the photocatalyst. Specifically, the variation at 494 nm corresponding to GSB signal is ascribed to the accumulation of photogenerated electrons at the conduction band minimum (CBM) of MoO_{3-x}, and their subsequent return to the ground state through excited emission and spontaneous emission. Besides, the variation at 511 nm corresponding to ESA signal is assigned to the generation of hot electrons and their relaxation back to the ground state. Fitting the kinetic traces at the bleach center (494 nm) in Supplementary Fig. 23, the hot electrons relaxation occurs within a few picoseconds, and the τ_1 (40.5 ps) of MoO_{3-x}/Ti_3C_2-OH is longer than that of MoO_{3-x} (38.8 ps). This indicates the vibration mode coupled with electron-phonon are weakened, which is beneficial for the electron transport process. The longer "survival time" of the LEF-induced hot electrons under illumination implies that more electrons can participate in the weakening of B-H in AB.

To eliminate the influence of temperature, the reactor is equipped with a recirculating cooling function to ensure that the catalytic reaction is performed at ~ 6 °C. As expected, the optimized MoO_{3-x}/Ti_3C_2-OH catalyst (Supplementary Figs. 24, 25) under full-light irradiation (Xenon lamp regulated to 100 $mW \cdot cm^{-2}$) exhibits the advisable photocatalytic activity as high as 11566.0 μmol $\cdot g^{-1} \cdot h^{-1}$, far exceeding the catalytic capacity of the single component and other multi-component photocatalysts (Fig. 4a). Subsequently, the deuterium-labeling experiments are conducted to verify the source of H_2. The result indicates that the H can be separately traced to AB and H_2O. As the

discussion of AIMD in Fig. 1g, the H_2O molecules are preferentially adsorbed onto AB for MoO_{3-x}/Ti_3C_2-OH. This favored configuration creates an optimal spatial arrangement, thereby enabling the rapid combination of two H atoms to form H_2 (Supplementary Fig. 26). For instance, the catalytic activity of the MoO_{3-x}/Ti_3C_2-OH is 6.6- and 6.3-fold that of the single plasmonic components Ti_3C_2-OH and MoO_{3-x}. It is also 6.9- and 8.4-fold that of the single component without plasmonic LEF effect Ti_3C_2 and MoO_3. In addition, the multi-component photocatalysts MoO_{3-x}/Ti_3C_2 and MoO_3/Ti_3C_2-OH composed of an individual LEF effect show a slight improvement, but the effect is more analogous to component mixing due to the absence of effective carrier transport channels. Even under NIR (Xenon lamp fitted with 800 nm filter) illumination in Fig. 4b, the MoO_{3-x}/Ti_3C_2-OH catalyst shows the equally brilliant performance with 3864 $\mu mol \cdot g^{-1} \cdot h^{-1}$, which is 5.7- and 6.1-fold compared to MoO_{3-x} and Ti_3C_2-OH, respectively. The MoO_{3-x}/Ti_3C_2-OH exhibits a significant catalytic enhancement under NIR illumination, owing to the existence of the hot electrons generated by the plasmon-coupling-induced strong LEF effect of between MoO_{3-x} and Ti_3C_2-OH. In addition, the LEF-induced photothermal effect on the local heating of the sample surface (Fig. 2b) is also investigated in the reaction process. Fig. 4c shows the catalytic activity of plasmon-coupling MoO_{3-x}/Ti_3C_2-OH photocatalysts under uncooled treatment with 158427.0 $\mu mol \cdot g^{-1} \cdot h^{-1}$. It is 13.7 times higher than that of the cooled treatment (~6 °C) under illumination, and is 148.3 times higher than that of thermocatalysis (45 °C) same as actual lighting temperature (Supplementary Fig. 27). The catalytic rate of the heterojunction sample without cooling treatment is 11.8 times that of Ti_3C_2-OH and 9.5 times that of MoO_{3-x}. Apparently, LEF-induced

photothermal effect could contribute to the catalytic efficiency of the dual-plasmonic reaction system, further accelerating the AB reaction.

To eliminate the effect of the light density (Xenon lamp), the photo-responsive catalytic activity of the heterojunction under single-band stimulation is investigated through apparent quantum yield (AQY) values. The intensity trend of the AQY coincides with the profile of the Vis-NIR light absorption curve of the catalysts (Supplementary Fig. 28). Specifically, the AQY value in the NIR region (> 800 nm) can also ~ 5%, confirming the source of the LEF-induced hot electrons. The stability of the photocatalytic hydrolysis of H_2 evolution from AB under simulated sunlight irradiation is evaluated under cooled treatment (~ 6 °C) (Fig. 4d). To eliminate the influence of AB concentration, the activity test of AB and performance comparison under different amounts of AB are conducted to determine the critical amount of consumed AB. The concentration of AB is ensured in an excess state during the whole reaction process (Supplementary Fig. 29). After 100 h irradiation, the MoO_{3-x}/Ti_3C_2-OH still exhibits the high catalytic activity, and the hydrogen production efficiency remain consistently at 9692 ~ 11854 $\mu mol \cdot g^{-1} \cdot h^{-1}$. Furthermore, MoO_{3-x}/Ti_3C_2-OH samples are collected after the cycle test, and the microstructural characterizations are presented in Supplementary Figs. 30 and 31. It suggests that the X-ray powder diffraction (XRD) pattern of post-react sample shows no obvious changes relative to that of fresh counterpart. The high resolution transmission electron microscope (HRTEM) images verify the intact structure in post-test MoO_{3-x}/Ti_3C_2-OH, representing the well structural stability against long-term irradiation. Finally, we compared the TOF of MoO_{3-x}/Ti_3C_2-OH in converting AB to hydrogen with the ever reported active sites of photocatalysts. As shown in Supplementary Figs.

32 and Supplementary Table 2, the TOF values of $Mo^{\delta+}$ active sites in MoO_{3-x}/Ti_3C_2-OH catalyst is as high as 5806 min^{-1}, delivering a great advantage over both non-noble and noble metal active sites ever reported. Apparently, the multi-field strategy enhanced $Mo^{\delta+}$ sites is highly effective in improving the dehydrogenation efficiency of AB hydrolysis.

We propose a multi-field coupling effect mechanism to elaborate the complete spatiotemporal evolution process from AB adsorption configuration to hydrolysis reaction. Firstly, the B atom in the AB molecules exhibits the most negative electrostatic potential (ESP) due to the presence of the surrounding electron pairs (Supplementary Fig. 33)[37]. The electron-deficient $Mo^{\delta+}$ atom is the most preferable reaction sites for capturing and activating the AB molecules. $Mo^{\delta+}$ also possesses both occupied and vacant orbitals, which is crucial for the fully activating AB. As displayed in Fig. 5a, the empty d orbitals of Mo accept the lone pair electrons of AB to form a stable adsorption configuration, while the occupied d orbitals of $Mo^{\delta+}$ transfer electrons in the opposite direction to the anti-bonding orbitals of AB to weaken the B-H bond. Both the "donate" and "feedback" bidirectional electron transfer processes can reduce the bond strength of the B-H bond. The differential charge result shows that the electron density increases between AB and Mo (Fig. 5a), indicating the formation of the Mo-B bond. The decrease in electron density occurs in the B-H bond region and behind the Mo atom, attributing to the electrons around Mo atom being pulled away to form a feedback bond. These feedback electrons enter the antibonding orbit of AB and thus weaken the B-H bond. This can also be confirmed by the enhancement of the bonding orbitals of Mo-B bond and the antibonding orbitals of the B-H bond in MoO_{3-x}/Ti_3C_2-OH (Fig. 5b)[38,39]. Therefore, feedback bond channel is the key factor in the breaking of the B-H bond. Then, a dark

AB hydrolysis experiment is carried out to verify the feedback bond channel effect. As shown in Supplementary Fig. 34, even in the absence of light, MoO_{3-x}/Ti_3C_2-OH still exhibits weak catalytic activity (690 $\mu mol \cdot g^{-1} \cdot h^{-1}$), due to the *d*-electrons of $Mo^{\delta+}$ reverse transfer to AB.

PEF effect can trigger the number of electrons around $Mo^{\delta+}$ by enhancing feedback channel, filling the B-H antibonding orbital (Fig. 5c). The electronic configuration and metal oxygen bond strength are evaluated by Crystal Orbital Hamilton populations (COHP). It is observed that the MoO_{3-x}/Ti_3C_2-OH has an increase of the integral of -COHP up to the Fermi level (ICOHP) of Mo-B bond to -4.39 eV and a decrease of the B-H ICOHP value to -0.83 eV compared to the MoO_3/Ti_3C_2 compound without PEF effect (Fig. 5b). Compared with MoO_3/Ti_3C_2, the *d*-band center of MoO_{3-x}/Ti_3C_2-OH shifts closer to the Fermi level, implying the improvement of adsorption capacity (Fig. 5d and Supplementary Fig. 35). According to Fig. 1g, the unique adsorption on surface of MoO_{3-x}/Ti_3C_2-OH restricts the direct contact of H_2O molecules. However, it strongly promotes the directional adsorption of AB molecules with enhanced adsorption of H_2O molecules on AB. The favored adsorption configuration induces the formation of a tight $NH_3BH_2^* \cdot H_2O$ transition complex, breaking the polarity of O-H bond, thereby significantly reducing the energy barrier for O-H bond break. Thus, the break of B-H bond during AB hydrolysis becomes the rate-determining step. To clarify the rate-determining step of AB hydrolysis, the kinetic isotope effect (KIE) is determined by calculating the ratio of rate constants for H_2O and D_2O (*i.e.*, k_H/k_D) based on non-competitive experiments (Supplementary Fig. 36). Apparently, AB in D_2O exhibits similar catalytic behavior to that of AB in H_2O, suggesting that the deuteron labelled D_2O has no direct effect on the production of H_2. A low KIE value of 1.05 belongs to a

typical secondary KIE, meaning that the D-O bond is not involved in the rate-determining step reaction. This illustrates the breakage of O-H is not a rate-determining step over the catalyst, although a part of H_2 comes from H_2O. Consequently, it is deduced that the slowest step in AB hydrolysis reaction should be the activation of B-H bond within AB[40,41]. This finding is different from the common AB hydrolysis reaction (without a catalyst and on pure MoO_{3-x} surface), where the rate-determining step is usually the break of O-H bond of H_2O molecules (Supplementary Fig. 37)[10,15]. For MoO_{3-x}/Ti_3C_2-OH composite system, the Gibbs free energy calculation in MoO_{3-x}/Ti_3C_2-OH indicates that the activation energy barrier of B-H bond (ΔE_2= 1.50 eV) is significantly higher than that of O-H bond (ΔE_4= 1.04 eV), implying the break of B-H bond becomes the rate-determining step for AB hydrolysis. The energies required for B-H bond cleavage (ΔE_2= 1.50 eV) and O-H bond break (ΔE_4 = 1.04 eV) in MoO_{3-x}/Ti_3C_2-OH are less than those in MoO_{3-x} (ΔE_2= 1.83, and ΔE_4 = 2.13 eV). These indicate that the PEF effect enhances feedback bond (Mo-B) and promotes B-H bond cleavage.

Under illumination, strong LEF effect can endow surface electrons with high energy to obtain hot electron, lowering the activation barrier of AB hydrolysis and making them easier to pump into the antibonding orbitals of the B-H bond (Fig. 5e). The *in-situ* FTIR spectra of the reaction medium are recorded at different reaction times. As shown in Fig. 5f, the characteristic vibration of the B-H bond at ~ 2361.0 cm^{-1} gradually weakens over times. A red-shift phenomenon can be observed at ~ 1080 and ~ 1175.5 cm^{-1}, corresponding to the B-H bond[10,42]. This time resolution of red-shift and the weakening of B-H bonds means the cleavage of B-H bonds as the reaction time increases[43]. Meanwhile, the N–H bonds at ~ 1402 and ~1620 cm^{-1} nearly remain unchanged. The breakage of

N-H bonds is not observed, impying that the H atom from the splitting of B–H bonds contributes to the hydrogen generation. Besides, the B-O bond signals can be hardly observed, indicating that there is almost no BO_2^- in the solution during the reaction process. This could remarkably inhibit the metal ions leaching caused by BO_2^- corrosion to enhance the stability. The Gibbs free energy of hydrogen adsorption (ΔG_{H^*}) under different electric fields is calculated to evaluate the desorption difficulty of the H^* arising from the breaking of the B-H bond. The MoO_{3-x}/Ti_3C_2-OH heterojunction approaches the equilibrium state (ΔG= -0.26 eV) under +0.02 eV/Å field (Fig. 5g), which is much lower than those of MoO_{3-x} (ΔG = -0.44 eV) and Ti_3C_2-OH (ΔG = -0.32 eV). These illustrates that LEF effect can dynamically optimize the H^* desorption from the catalyst surface, ultimately forming the hydrogen molecules. Simultaneously, $Mo^{\delta+}$ active sites are released, thereby initiating the next reaction cycle.

Discussion

In summary, we have demonstrated a strategy, as exemplified by a MoO_{3-x}/Ti_3C_2-OH heterojunction, to enhance AB hydrolytic activity, which is accomplished by plasmon polarization induced multi-field coupling. Encouraged by the ML and AIMD theoretical results, the engineered $Mo^{\delta+}$ active sites facilitate the directional adsorption and structural distortion of AB, thereby simplifying the reaction pathway and shortening the hydrogen migration distance. The reconstructed $Mo^{\delta+}$ active site of MoO_{3-x}/Ti_3C_2-OH demonstrates decent stability over 100 h and well performance with a TOF of 5806 min^{-1}, showing competitiveness compared to the reported non-noble and noble-metal based catalysts. This enhanced performance mainly stems from the multi-field synergistic effect. PEF drives charge carrier separation in the catalyst, leading to

electron accumulation at $Mo^{\delta+}$ active sites. Strong LEF endows surface electrons with high energy, enabling hot electrons to be pumped into the antibonding orbital of the B-H bond, ultimately reducing the high reaction energy barrier of AB hydrolysis. This work not only provides valuable insights for designing atomic-level active sites for efficient hydrogen production, but also offers inspiration on developing high-performance catalysts for hydrogen production.

Methods

Synthesis of MoO_{3-x}

Following a procedure adapted from previously reported methods[44], molybdenum powder (60 mg) was dispersed in 20 mL ethanol and stirred for 20 min. Subsequently, 0.94 mL H_2O_2 was added dropwise to the mixture, followed by another 20 min stirring. The resulting solution was then transferred into a polytetrafluoroethylene reactor and maintained at 160 °C for 12 h. After the reactor had cooled naturally to room temperature, the solid product was collected by centrifugation, washed repeatedly with absolute ethanol, and a blue-black precipitate was obtained. This precipitate was finally dried in a vacuum oven at 60 °C for 12 h.

Synthesis of Ti_3C_2

2 g Ti_3AlC_2 was added into 20 mL HF, then placed in an oil bath and heated to 65 ℃ and stirred for 200 minutes. After the reaction, this solution was subjected to repeated centrifugation and washing, repeating eight times. The washed solution was placed in the refrigerator for 5 h, then taken out and placed in a freeze dryer to dry for 24 h to obtain Ti_3C_2.

Synthesis of Ti_3C_2-OH

3 mg of Ti_3C_2 was weighed and 20 mL of ultrapure water was added, sonicated for 20 min, then

0.5 mL of ammonia was dropped and shaken evenly. The mixture was then transferred to a polytetrafluoroethylene reactor and placed in an oven at 150 °C for 24 h. After the reactor was reduced to room temperature, took it out and put it in the refrigerator for 3 h. It was then put into a freeze dryer to dry overnight to obtain a yellowish solid.

Synthesis of MoO_{3-x}/Ti_3C_2-OH

4 mg Ti_3C_2-OH and 16 mg MoO_{3-x} was weighed, the Ti_3C_2-OH was first sonicated in 15 mL of absolute ethanol, and then MoO_{3-x} was dispersed in the ethanol solution of the Ti_3C_2-OH. After the mixture was stirred and mixed for 2 hours, it was allowed to stand and deposited overnight.

Characterization methods

The crystalline structure of the samples was characterized using X-ray powder diffraction (XRD, D8 Advance, Bruker, Germany) with Cu Kα radiation (λ = 1.5406 Å). Microstructures including surface and internal morphologies were examined via scanning electron microscopy (SEM, S-4800, Hitachi, Japan) and transmission electron microscopy (TEM, JEOL JEM-2100, Japan). Using a Mg Kα ADES source (hν = 1253.6 eV) under ultrahigh vacuum (< 10^{-8} Pa), X-ray photoelectron spectroscopy (XPS, Thermo ESCALAB 250Xi, USA) was employed to analyze the surface chemical composition and elemental valence states. Optical absorption properties in the UV-Vis-IR range were measured using a Lambda 750 UV-Vis-IR spectrophotometer (U-3900, HITACHI, Japan). The photoluminescence (PL) spectra were acquired at room temperature on a fluorescence spectrophotometer (Fluromax-4P, Horiba Jobin Yvon, France)[45]. Room-temperature electron paramagnetic resonance recorded at 300 K and 9.86 GHz on a Bruker A300 EPR spectrometer demonstrated the presence of oxygen defects in MoO_{3-x} and a decrease in oxygen defect

concentrations after composite Ti_3C_2-OH. The surface potentials of catalyst were analyzed by Zeta potentiometer (Nano ZS90, Malvern, Britain).The femtosecond transient absorption spectrometer (Helios, Ultrafast Systems, USA) was used to explore the electron relaxation dynamics in MoO_{3-x} and MoO_{3-x}/Ti_3C_2-OH in detail. Fourier Transform Infrared Spectroscopy (FTIR, INVENIO S, Bruker, Germany) equipped with a Deuterated L-alaninedoped TriGlycine Sulphate (DLaTGS) infrared detector was used for conventional infrared spectroscopy measurements, and that equipped with a liquid nitrogen-cooled mercury cadmium telluride (MCT) infrared detector was used for *in-situ* FTIR measurements. The X-ray absorption fine structure (XAFS) measurements were conducted on a Rapid XAFS HE Ultra system (Anhui Absorption Spectroscopy Analysis Instrument Co., Ltd.), collected in transmission (or fluorescence) mode[46].

Hydrogen evolution experiment

The photocatalytic hydrogen evolution experiments were carried out using an online gas analysis system (Labsolar 6A, Perfectlight, Beijing). A 300 W Xenon lamp (CEL-HXF300, Ceaulight, Beijing) equipped with or without an 800 nm cut-off filter was employed as the light source to simulate sunlight or to provide near-infrared (NIR) illumination, respectively. The system also included a vacuum pump, gas sampling unit, circulation pump and condensers. In a typical run, 10 mg photocatalyst and 33 mg NH_3BH_3 were dispersed in 100 mL deionized water under ultrasonic treatment to ensure uniform suspension. The mixture was then transferred into a quartz reactor and degassed thoroughly with a vacuum pump for 30 min to eliminate any dissolved gases. Afterwards, the reactor was irradiated with the Xenon lamp to initiate the AB hydrolysis reaction. The evolved gases were periodically swept into a gas chromatograph (GC7920, Ceaulight, Beijing) for

composition analysis, and trace amounts of by-products such as O_2 were detected during the process. The catalytic hydrolysis of NH_3BH_3 using a suitable catalyst for hydrogen production was carried out according to the following equation.

$$NH_3BH_3 + 2H_2O \xrightarrow{\text{catalyst}} NH_4^+ + BO_2^- + 3H_2$$

(1)

Apparent quantum yield (AQY) was evaluated by the following formula.

$$AQY = \frac{2\times R}{I} \times 100\% = \frac{N_A \times c \times E_\lambda \times 2}{I \times A} \times 100\%$$

(2)

I and R were the incident photons and the number of H_2 molecules produced at the same time, c was the speed of hydrogen production, N_A was the Avogadro constant, I was the optical power density, A was the incident light area, and E_λ was the energy of one photon upon λ wavelength, respectively. The test conditions for AQY were the same as those for photocatalytic hydrogen evolution, excepting that the lamp source was changed to a 300 W Xenon lamp with a filter with a specific wavelength. For example, upon 420 nm wavelength excitation corresponding to 2.95 eV, the optical power density was 8.96 $W \cdot m^{-2}$, the incident light area was 66.5 cm^2, and the related hydrogen production rate was 374.2 $\mu mol \cdot g^{-1} \cdot h^{-1}$, and the AQE value was 0.997%, according to equation (2). The AQE values for each wavelength were determined by three independent measurements, with an error of ±0.008%.

In addition, turnover frequency (TOF) was defined as the amount of AB converted active site per unit of time, and it was the core parameter to measure the efficiency of the catalyst in converting AB to hydrogen. The TOF value (min^{-1}) was calculated based on the number of active sites in the

catalyst. The calculation equation used was as below:

$$TOF = \frac{n_{H_2}}{t \times n_{Mo^{\delta+}}}$$

(3)

Wherein, n_{H_2} represents the moles of the generated hydrogen and t was the reaction time. $n_{Mo^{\delta+}}$ represented the molar of $Mo^{\delta+}$ obtained through EPR electron spin measurement.

Hydrogen production cycle test

10 mg as-prepared MoO_{3-x}/Ti_3C_2-OH photocatalyst was dispersed in 100 mL ultrapure water, and 400 mg NH_3BH_3 was added to the suspension. The mixture was fully homogenized by magnetic stirring for 30 min to ensure uniform dispersion of the catalyst and complete dissolution of NH_3BH_3. The uniformly mixed suspension was transferred to a customized quartz reactor with a cooling water circulation pump (CEL-UC5, Ceaulight). The air inside the sealed reactor was evacuated by a vacuum pump (<10 Pa). After evacuation, high-purity Ar gas (99.999%) was introduced into the reactor to maintain an inert atmosphere (0.1 MPa), which was kept constant throughout the test to avoid the interference from oxygen or moisture in the air. The durability test was carried out using the same 300 W Xenon lamp (CEL-HXF300 Ceaulight) as the simulated sunlight source (100 $mW \cdot cm^{-2}$) with continuous irradiation. The optical power of the Xenon lamp during the cycle was directly measured by optical power meter (THORLABS, CELISS, Tianjin) with energy probe (PM100D, CELISS, Tianjin), assuring this power stability and light intensity remained at around 100 $mW \cdot cm^{-2}$ and 21 A, respectively (Supplementary Table 3). The temperature of the reaction system was controlled at 6 °C by the reactor connected to condensers (cooling water circulation pump: CEL-UC5, Ceaulight) to eliminate the influence of temperature

fluctuations on catalytic activity. The hydrogen gas produced during the reaction was continuously delivered to the online gas chromatograph (GC7920, Ceaulight, Beijing) at intervals of 0.5 h for quantitative analysis (detection conditions: thermal condu ctivity detector (TCD), Ar carrier gas, column temperature: 50 °C). The catalytic activity (hydrogen production efficiency) was calculated in real time based on the GC detection results, and the test was continuously performed for 100 h without interrupting the light source or replacing the catalyst and reactants (Supplementary Fig. 38).

Thermocatalytic reaction

10 mg photocatalyst was combined with 33 mg NH_3BH_3 in 100 mL deionized water and subjected to ultrasonic treatment to achieve a homogeneous dispersion. The resulting suspension was transferred into a reactor, which was then put in a water bath device with 45 °C. Prior to the reaction, the system was degassed about 30 min using a vacuum pump. Subsequently, the mixture was kept in the dark at 45 °C for 3 h to establish a stable hydrolysis rate per hour.

Fourier Transform Infrared Spectroscopy (FTIR) measurements

In-situ FTIR measurements: *In-situ* FTIR experiments were performed using an INVENIO S spectrometer equipped with a liquid nitrogen-cooled mercury cadmium telluride (MCT) infrared detector. 10 mg of catalyst and 33 mg AB were dissolved in 100 mL of deionized water, fully dispersed after 10 min of sonication. Then 10 mL of the dispersion was placed in an *in-situ* reaction tank. Prior to analysis, Ar gas was continuously injected into the reaction solution at a flow rate of 20 $ml \cdot min^{-1}$ for 30 min. Subsequently, the *in-situ* FTIR spectra were recorded at room temperature and atmospheric pressure for 35 min using 300 W Xenon lamps as the light source. All spectra

were subject to background subtraction and baseline calibration, and the spectra were collected in the range of 4000-400 cm^{-1} with a resolution of 8 cm^{-1} and 32 scans.

FITR measurements: FTIR experiments were performed using an INVENIO S spectrometer equipped with a Deuterated L-alaninedoped TriGlycine Sulphate (DLaTGS) infrared detector. 10 mg catalyst powder was mixed evenly with 50 mg KBr powder, and pressed into a translucent lamella using a tablet press. Subsequently, the translucent lamella was placed in the sample chamber optical path of infrared spectrometer to collect the infrared spectrum. All spectra were subject to background subtraction and baseline calibration, and the spectra were collected in the range of 4000-400 cm^{-1} with a resolution of 8 cm^{-1} and 32 scans.

Photoelectrochemical measurements

The photoelectrochemical properties were tested at room temperature by electrochemical workstation (CHI 760F, Chenhua, Shanghai). Specifically, 1L 0.5 M Na_2SO_4 (PH≈ 7) electrolyte solution was prepared by dissolving 71.1 g of Na_2SO_4 in 1 L ultrapure water, which was tested in a conventional three-electrode cell. Ag/AgCl and Pt were used as the reference and counter electrodes, respectively. During the electrochemical test, the calibrated voltage value of Ag/AgCl was -0.201 V. For working electrode preparation via drop-coating, a suspension was initially formulated by dispersing 5 mg photocatalyst and 50 μL Nafion in 1 mL ethanol. This resulting suspension was subsequently applied onto an indium tin oxide (ITO) glass electrode with a defined exposed area of 1 cm^2, and the coated electrode was then placed in an oven for drying. A 300 W Xenon lamp fitted with a solar simulator filter served as the illumination source, with the light intensity set to 100 $mW \cdot cm^{-2}$. The CV and LSV measurements presented in Fig. 2g and 3d were

performed without iR correction.

Finite-element modeling simulations

To explore the local electric field enhancement arising from the LSPR effect in plasmonic nanostructures (specifically MoO_{3-x}, Ti_3C_2-OH, and their heterojunction MoO_{3-x}/Ti_3C_2-OH), we performed three-dimensional finite element method (FEM) simulations on these material systems. The simulations were conducted under ultraviolet excitation conditions (frequency set as $3\times e^8/\lambda\times e^{-9}$), with the samples embedded in a homogeneous medium characterized by a specific refractive index. The background electromagnetic field, corresponding to an incident plane wave, was determined by using the Wave Optics Module based on the following equations:

$$E_b = E_0 e^{i(\omega t - \boldsymbol{k}\cdot T)} \quad (4)$$

In general, **k** was in the X-Y plane, and the angle θ between **k** and Z was given. The MoO_{3-x}/Ti_3C_2-OH heterojunction was simplified into several interlaced MoO_{3-x} nanosheets (thickness = 4 nm) and dozens of Ti_3C_2-OH (diameter = 8 nm). The appropriate size was selected to represent the relative position of the two components. Format with non-uniform format objects, where the maximum value was less than $\lambda/6$, and used a covering grid cell size of 1×1 nm^2. A perfectly matched layer (PML) was required to minimize scattering at the outer boundaries. The sample required for the simulation was placed in the X-Y plane, and the incident light of any wavelength was selected to propagate in the Z direction, and the velocity polarization of 5 V/m was selected in the X, Y and Z directions, respectively. Therefore, the optimal polarization direction was selected as the Y direction. The incident light (420 nm, 600 nm, 800 nm, 980 nm) was then selected

to propagate in the Z direction and polarized at a rate of 5 V/m in the Y direction, resulting in an optimal incidence wavelength of 800 nm.

DFT calculations

The electronic structure calculations were carried out using density functional theory (DFT) implemented in the Vienna Ab initio Simulation Package (VASP). The Perdew-Burke-Ernzerhof (PBE) functional under the generalized gradient approximation (GGA) was utilized to treat the exchange-correlation potential. To properly account for the strong on-site Coulomb repulsion among localized d electrons in transition metal systems, the DFT+U approach was employed for the d orbitals of Ti and Mo. This method incorporates a Hubbard-type correction into the conventional DFT Hamiltonian to better describe the correlated electronic states arising from narrow bands[47,48]. The on-site Coulomb interactions for the transition metal ion were expressed as U_{eff} = 6 eV for Mo ions and U_{eff} = 3 eV for Ti ions, respectively. During structural optimizations of the surface models, a 3× 3 × 1 gamma-point was used. The (002) facet of MoO_{3-x} and the (002) facet of Ti_3C_2-OH were selected for DFT calculations. The optimized structure of MoO_{3-x} (a = 11.08920 Å, b = 11.88840 Å, c = 6.13497 Å, and α = β = γ = 90°) and Ti_3C_2-OH (a = 3.069 Å, b = 3.069 Å, c = 7.130 Å, and α = β = 90°, γ = 120°) were obtained (Supplementary Fig. 39). To ensure the structural stability of heterojunction model during the geometric optimization and electronic structure calculation, the Ti_3C_2-OH was subjected to crystal system transformation with α = β = γ = 90°. Subsequently, the MoO_{3-x} and Ti_3C_2-OH cells were expanded, resulting in a lattice mismatch of less than 0.2%. The layer spacing was set to 2.5 Å in MoO_{3-x}/Ti_3C_2-OH heterojunction model (Supplementary Fig. 40). A vacuum of 25 Å was used to eliminate false interactions. The plane

wave energy cutoff was fixed to 400 eV. All structures of these materials (see Supplementary Data 1) were optimized, the structure was fully relaxed until the changes in energy and force reach 1×10^{-4} eV and 0.01 eV·Å^{-1}, respectively. After structure optimization, catalytic properties were evaluated by calculating the Gibbs free energy for H* adsorption:

$$\Delta G_{H*} = E_{sur-H} - E_{sur} - E_{\frac{1}{2}H_2} + \Delta E_{ZPE} - T\Delta S$$

(5)

Here, E_{sur-H} and E_{sur} were the total energies of the surface with and without adsorbed hydrogen, respectively, while E_{H_2} was the energy of a hydrogen molecule in the gas phase. ΔE_{ZPE} and ΔS accounted for the changes in zero-point energy and entropy. In AIMD simulations, the Nose-Hoover thermostat in the canonical (NVT) ensemble was used to control temperature and pressure, with a time step of 1.0 femtoseconds, conducted at a finite temperature of 300 K for over 200 ps. Our DFT calculations employed idealized models, which cannot fully capture the inherent structural complexity and dynamic nature of the real systems.

Machine Learning computational details

A model was constructed for predicting the Gibbs free energy (ΔG_{H*}) of hydrogen production when AB adsorbs metal sites using machine learning (ML) methods. 86 sets of data covering different metal active sites, involving 13 original features with their corresponding Gibbs free energy, were collected and analyzed. Here, a definition of the concentration of carriers p was proposed to better fit the process of photocatalysis and amplify the feature space. Random Forest algorithm was adopted to eliminate features weakly correlated to the target, and just retain the key descriptor features to improve the accuracy of the model. Then, four algorithms (Fine Gaussian

SVM, Matern 5-2 GPR, Second rational GPR and Average index GPR) were used to establish ΔG_{H^*} prediction models. To verify the reliability of the model, a five-fold cross-validation framework was adopted, obtaining two indexes to describe the predicting error (RMSE and R^2). The indexes were used to evaluate the accuracy of model performance.

Data availability

All data generated in this study are provided in the Supplementary Information/Source Data file. The data that support the findings of this study are available from the corresponding author upon request. Source data are provided with this paper.

References

1. Fu, H. et al. A scalable solar-driven photocatalytic system for separated H_2 and O_2 production from water. *Nat. Commun.* **16**, (2025).
2. Guo, S. et al. Boosting photocatalytic hydrogen production from water by photothermally induced biphase systems. *Nat. Commun.* **12**, (2021).
3. Jin, S. et al. 2D MoB MBene: An Efficient Co-Catalyst for Photocatalytic Hydrogen Production under Visible Light. *ACS Nano.* **18**, 12524-12536 (2024).
4. Liu, Y. et al. Cu_2O/2D COFs Core/Shell Nanocubes with Antiphotocorrosion Ability for Efficient Photocatalytic Hydrogen Evolution. *ACS Nano.* **17**, 5994-6001 (2023).
5. Xu, W. et al. Metal/metal-organic framework interfacial ensemble-induced dual site catalysis towards hydrogen generation. *App. Catal. B: Environ.* **286**, 119946 (2021).
6. Khanam, S., Rout, S.K. Plasmonic Metal/Semiconductor Heterostructure for Visible Light-Enhanced H_2 Production. *ACS Omega.* **7**, 25466-25475 (2022).
7. Rej, S. et al. Facet-Dependent and Light-Assisted Efficient Hydrogen Evolution from Ammonia Borane Using Gold-Palladium Core-Shell Nanocatalysts. *Angew. Chem. Int. Ed.* **55**, 7222-7226 (2016).
8. Shao, W. et al. Symmetry Breaking in Monometallic Nanocrystals toward Broadband and Direct Electron Transfer Enhanced Plasmonic Photocatalysis. *Adv. Funct. Mater.* **31**, (2020).
9. Song, J. et al. Remarkably boosting catalytic H_2 evolution from ammonia borane through the visible-light-driven synergistic electron effect of non-plasmonic noble-metal-free nanoparticles and photoactive metal-organic frameworks. *App. Catal. B: Environ.* **225**, 424-432 (2018).
10. Zhang, S. et al. Visible-Light-Driven Multichannel Regulation of Local Electron Density to Accelerate Activation of O-H and B–H Bonds for Ammonia Borane Hydrolysis. *ACS Catal.* **10**, 14903-14915 (2020).
11. Chen, W. et al. Restructuring the interfacial active sites to generalize the volcano curves for platinum-cobalt synergistic catalysis. *Nat. Commun.* **15**, (2024).
12. Chen, Y. et al. Practical H_2 supply from ammonia borane enabled by amorphous iron domain. *Nat. Commun.* **15**,

(2024).

13. Wan, C. et al. Silica Confinement for Stable and Magnetic Co-Cu Alloy Nanoparticles in Nitrogen-Doped Carbon for Enhanced Hydrogen Evolution. *Angew. Chem. Int. Ed.* **63**, (2024).
14. Li, Y. et al. Ruthenium Nanoparticles Anchored on Cobalt Oxide Married with Nitrogen and Phosphorus Co-Doped Carbon for Hydrolytic Dehydrogenation of Ammonia Borane. *ACS Catal.* **15**, 9158-9170 (2025).
15. Fu, F. et al. Highly Selective and Sharp Volcano-type Synergistic Ni_2Pt@ZIF-8-Catalyzed Hydrogen Evolution from Ammonia Borane Hydrolysis. *J.Am.Chem.Soc.* **140**, 10034-10042 (2018).
16. Guan, S. et al. Efficient Hydrogen Generation from Ammonia Borane Hydrolysis on a Tandem Ruthenium-Platinum-Titanium Catalyst. *Angew. Chem. Int. Ed.* **63**, (2024).
17. Xie, S. et al. Synergizing Mg Single Atoms and Ru Nanoclusters for Boosting the Ammonia Borane Hydrolysis to Produce Hydrogen. *Angew. Chem. Int. Ed.* **64**, (2025).
18. Zhu, A. et al. Geminal Synergy in Pt-Co Dual-Atom Catalysts: From Synthesis to Photocatalytic Hydrogen Production. *J.Am.Chem.Soc.* **146**, 33002-33011 (2024).
19. Li, J. et al. Sub-2 nm Ternary Metallic Alloy Encapsulated within Montmorillonite Interlayers for Efficient Hydrogen Generation from Ammonia Borane Hydrolysis. *ACS Catal.* **14**, 14665-14677 (2024).
20. Shen, J. et al. Efficient Generation of Negative Hydrogen with Bimetallic-Ternary-Structured Catalysts for Nitrobenzene Hydrogenation. *Angew. Chem. Int. Ed.* **64**, (2025).
21. Wen, M. et al. Non-Noble-Metal Nanoparticle Supported on Metal-Organic Framework as an Efficient and Durable Catalyst for Promoting H_2 Production from Ammonia Borane under Visible Light Irradiation. *ACS Appl. Mater. Interfaces.* **8**, 21278-21284 (2016).
22. Yang, X.J. et al. Non-noble metallic nanoparticles supported on titania spheres as catalysts for hydrogen generation from hydrolysis of ammonia borane under ultraviolet light irradiation. *Int. J. Hydrog. Energy.* **43**, 16556-16565 (2018).
23. Guo, J. et al. Graphene supported Pt-Ni bimetallic nanoparticles for efficient hydrogen generation from KBH_4/NH_3BH_3 hydrolysis. *Int. J. Hydrog. Energy.* **47**, 11601-11610 (2022).
24. Liu, K. et al. Enhanced catalytic behavior of h-BN supported CuNi bimetallic catalysts in hydrolytic dehydrogenation of NH3BH3. *Int. J. Hydrogen Energy.* **47**, 33741-33753 (2022).
25. Wang, Y. et al. Co-Mo-B nanoparticles supported on carbon cloth as effective catalysts for the hydrolysis of ammonia borane. *Int. J. Hydrogen Energy.* **45**, 14418-14427 (2020).
26. Yang, H. et al. One-Pot MOFs-Encapsulation Derived In-Doped ZnO@In_2O_3 Hybrid Photocatalyst for Enhanced Visible-Light-Driven Photocatalytic Hydrogen Evolution. *Adv. Sustain. Syst.* **7**, 2200443-2200454 (2022).
27. Liu, X. et al. Full-spectrum plasmonic semiconductors for photocatalysis. *Mater. Horiz.* **11**, 5470-5498 (2024).
28. Guo, J. et al. Boosting Hot Electrons in Hetero-superstructures for Plasmon-Enhanced Catalysis. *J.Am.Chem.Soc.* **139**, 17964-17972 (2017).
29. Pan, L. et al. Boosting the performance of Cu_2O photocathodes for unassisted solar water splitting devices. *Nat. Catal.* **1**, 412-420 (2018).
30. T. Hertel, E.K., M. Wolf, and G. Ertl. Ultrafast Electron Dynamics at Cu(111): Response of an Electron Gas to Optical Excitation. *Phys. Rev. Lett.* **76**, 535-538 (1996).
31. Jose. H. Hodak, I.M., and Gregory V. Hartland. Spectroscopy and Dynamics of Nanometer-Sized Noble Metal Particles. *J. Phys. Chem. B.* **102**, 6958-6967 (1998).
32. Chu, K. et al. Unveiling the Synergy of O-Vacancy and Heterostructure over MoO_{3-x}/MXene for N_2 Electroreduction to NH_3. *Adv. Energy Mater.* **12**, (2021).

33. Zhu, Q. et al. Hydrogen-Doping-Induced Metal-Like Ultrahigh Free-Carrier Concentration in Metal-Oxide Material for Giant and Tunable Plasmon Resonance. *Adv. Mater.* **32**, (2020).
34. Yu, Y. et al. Surface Engineering for Extremely Enhanced Charge Separation and Photocatalytic Hydrogen Evolution on g-C_3N_4. *Adv. Mater.* **30**, (2018).
35. Dou, M. et al. Qualitative and quantitative analysis of electrons donated by pollutants in electron transfer-based oxidation system: Electrochemical measurement and theoretical calculations. *J. Hazard. Mater.* **473**, 134720-134732 (2024).
36. Qu, Z. et al. Designing C-Fe-O bonded MIL-88B(Fe)/jasmine petal-derived-carbon composite biosensor for the simultaneous detection of dopamine and uric acid. *Chem. Eng. J.* **404**, 126570-126630 (2021).
37. Shiroudi, A. et al. Computational analysis of substituent effects on proton affinity and gas-phase basicity of TEMPO derivatives and their hydrogen bonding interactions with water molecules. *Sci. Rep.* **14**, 1-20 (2024).
38. Dai, T.Y. et al. Recent Progress on Computation-Guided Catalyst Design for Highly Efficient Nitrogen Reduction Reaction. *Adv. Funct. Mater.* **34**, 2400773-2400793 (2024).
39. Zhang, S. et al. Photocatalytic H_2 Evolution from Ammonia Borane: Improvement of Charge Separation and Directional Charge Transmission. *ChemSusChem.* **13**, 5264-5272 (2020).
40. Li, Z. et al. Covalent triazine framework supported non-noble metal nanoparticles with superior activity for catalytic hydrolysis of ammonia borane: from mechanistic study to catalyst design. *Chem. Sci.* **8**, 781-788 (2017).
41. elville, H.W.M. et al. The Sorption of Hydrogen and Deuterium by Copper and Palladium I-The Behaviour of Copper and Copper Oxides. *Proc. R. Soc. A.* **151**, 77-88 (1935).
42. Zhang, C. et al. Two-dimensional molybdenum boride coordinating with ruthenium nanoparticles to boost hydrogen generation from hydrolytic dehydrogenation of ammonia borane. *J. Colloid Interface Sci.* **669**, 794-803 (2024).
43. Zheng, J.-H. et al. General strategy for evaluating the d-band center shift and ethanol oxidation reaction pathway towards Pt-based electrocatalysts. *Sci. China Chem.* **66**, 279-288 (2022).
44. He, Y. et al. Double-plasmonic-coupled heterojunction photocatalysts for highly-efficient full-spectrum-light-driven H_2 evolution from ammonia borane. *Chem. Eng. J.* **481**, 148299-148311 (2024).
45. Xie, Z. et al. Rationally-designed core-shell structure with double-plasmon effect for efficient and tunable upconversion luminescence emission. *Appl. Surf. Sci.* **643**, 158726-158736 (2024).
46. Sun, G. et al. Structural design and electronic regulation of atomically dispersed Mo-S_4 sites by second shell N species reconfiguration for intensifying hydrogen spillover. *Chem. Eng. J.* **500**, 156679-156687 (2024).
47. Su, D. et al. Efficient amine-assisted CO_2 hydrogenation to methanol co-catalyzed by metallic and oxidized sites within ruthenium clusters. *Nat. Commun.* **16**, 590-600 (2025).
48. Rohrbach, A., Hafner, J. Molecular adsorption of NO on NiO(100): DFT andDFT+Ucalculations. *PRB.* **71**, 1-7 (2005).

Acknowledgements

The authors acknowledge the financial support from the National Natural Science Foundation of China (NSFC, Grant No. 62205165, 52102362, 51672143, 51808303).

Author contributions

Y. Y., D. Y. and W. Y. conceived the idea and directed the project. P. Li performed the synthesis of the samples, material characterizations, experimental measurement and data analysis. N. Tu conducted the theoretical calculations and data analysis. J. Li gave the assistance with data collection. H. Hou analyzed and discussed the results. Y. Y., D. Y. and W. Y. carried out the data analyses and cowrote the manuscript. All authors discussed the data and contributed to the manuscript.

Competing interests

The authors declare no competing interests.

Figure Legends/Captions (for main text figures)

Fig. 1 | Design concept and theoretical calculation. a Schematic diagram of photocatalytic AB hydrolysis with different metal active sites. The red dashed circle indicates the location of H atom that breaks the bond in the AB or H_2O molecule. **b** Heat map inferred by Pearson's correlation coefficient. **c** Predictive response for Fine gaussian SVM. **d** Feature importance analysis. **e-f** Molecular dynamic process of AB water solution after 10 ps of MoO_{3-x} and MoO_{3-x}/Ti_3C_2-OH. **g** RDF curves of AB water solution interactions, inset shows the atomic structure of AB on the MoO_{3-x}/Ti_3C_2-OH catalyst surface.

Fig. 2 | Characterization and polarization effect in MoO_{3-x}/Ti_3C_2-OH heterojunction. a Normalized Mo K-edge XANES spectra of MoO_{3-x}, MoO_{3-x}/Ti_3C_2-OH along with reference materials Mo foil, MoO_2 and MoO_3. **b** FT and **c** WT k^3-weighted $\chi(k)$-function of the EXAFS spectra. **d** 2D cross sectional view of differential charge density of MoO_3/Ti_3C_2 and MoO_{3-x}/Ti_3C_2-OH. **e** Dipole moment and ΔV value of different samples. **f** Average electrostatic potential distribution (V) of MoO_{3-x}/Ti_3C_2-OH along the out-of-plane direction. **g** CV curves of different samples. **h** 3D atomic force microscopy image and **i** surface potential, surface charge density and

relative IEF intensity of Ti_3C_2-OH, MoO_{3-x} and MoO_{3-x}/Ti_3C_2-OH.

Fig. 3 | Characterization and electric field effect of double plasmonic system. a Electric field distributions and thermal imaging after the temperature reached steady values of MoO_{3-x} and MoO_{3-x}/Ti_3C_2-OH under 800 nm excitation. **b-c** Surface potential of MoO_{3-x}/Ti_3C_2-OH under different light irradiation. **d** LSV polarization curves under different condition for MoO_{3-x}/Ti_3C_2-OH photoelectrodes recorded in Na_2SO_4 electrolyte. **e** Differential charge density of MoO_{3-x}/Ti_3C_2-OH under different electric field gradient. **f** Ultrafast TA spectra of MoO_{3-x} and MoO_{3-x}/Ti_3C_2-OH after 420 nm excitation. **g** Representative spectra at different delay time for MoO_{3-x}/Ti_3C_2-OH.

Fig. 4 | AB hydrolysis performance. Photocatalytic H_2 production activities of different samples **a** under full-light irradiation and **b** under NIR light irradiation. **c** Catalytic activity of Ti_3C_2-OH, MoO_{3-x} and MoO_{3-x}/Ti_3C_2-OH under cooled and uncooled measure. **d** Cycling curves of MoO_{3-x}/Ti_3C_2-OH photocatalyst. The photos in the picture are recorded at different time during the cycling test period.

Fig. 5 | Multi-field-mediated AB hydrolysis mechanism. a "Donate-feedback" channel for B-H bonding to Mo and differential charge density of MoO_{3-x}/Ti_3C_2-OH-AB. The blue dashed circle represents the magnified local charge density difference. **b** COHP of the Mo-B bond in MoO_3/Ti_3C_2-AB and MoO_{3-x}/Ti_3C_2-OH-AB, and the B-H bond in AB and MoO_{3-x}/Ti_3C_2-OH-AB. **c** Diagram of the formation of PEF effect in the MoO_{3-x}/Ti_3C_2-OH. **d** Schematic diagram about the PEF-enhanced AB adsorption on $Mo^{\delta+}$ sites. **e** Diagram of the formation and impact of LEF effect on $Mo^{\delta+}$ sites. The arrows represent the generation of hot electrons near the $Mo^{\delta+}$ site and the injection of hot electrons into the AB antibonding orbitals. **f** *In-situ* FTIR spectra of AB hydrolysis catalyzed by MoO_{3-x}/Ti_3C_2-OH. **g** Gibbs free energy of different catalysts under different electric field gradient.

Editorial Summary:

The authors find that reconstructing the Moδ+ active site via multi-field coupling effectively boosts ammonia borane hydrolysis. They provide key insights into the plasmon polarization-induced carrier kinetics and hydrolysis mechanism.

Peer Review Information: *Nature Communications* thanks Yu-Jia Zeng and the other anonymous, reviewer(s) for their contribution to the peer review of this work. A peer review file is available."

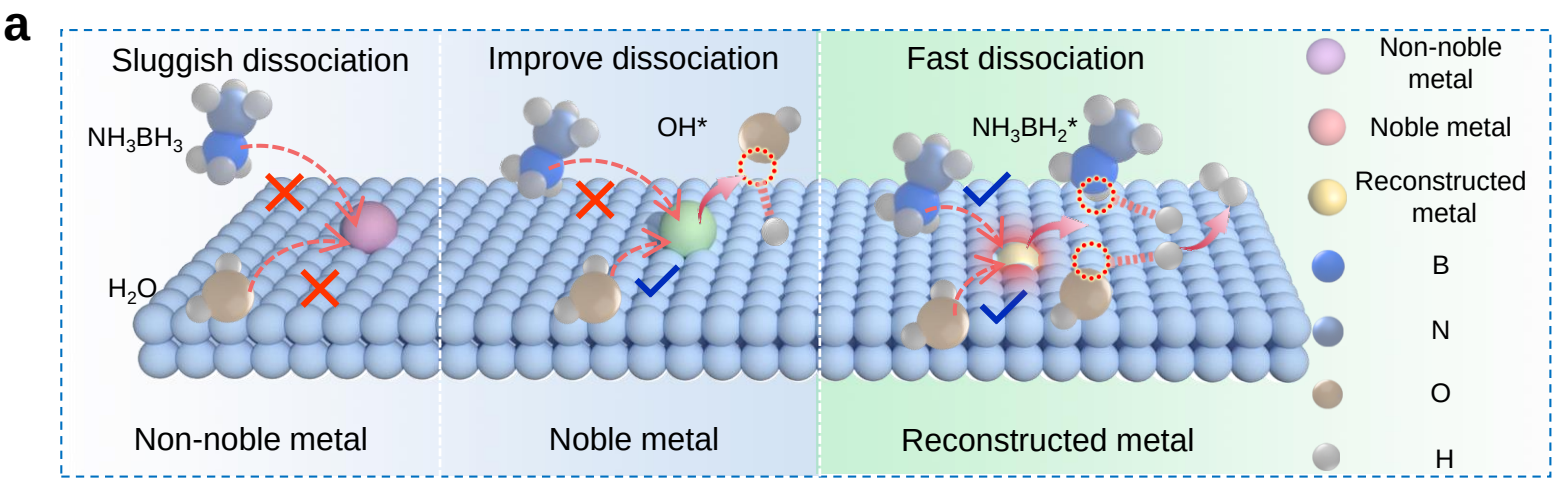
a
Sluggish dissociation
Improve dissociation
Fast dissociation
NH_3BH_3
H_2O
OH*
NH_3BH_2*
Non-noble metal
Noble metal
Reconstructed metal
Non-noble metal
Noble metal
Reconstructed metal
B
N
O
H

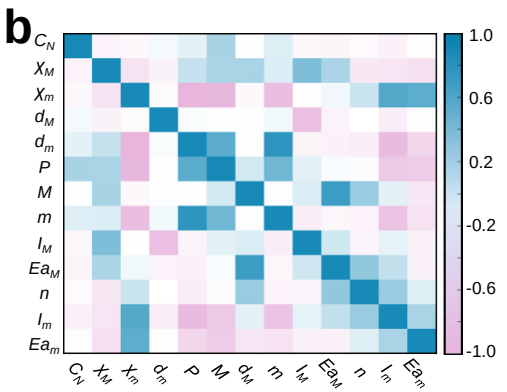
b
C_N
X_M
X_m
d_M
d_m
P
M
m
I_M
Ea_M
n
I_m
Ea_m
1.0
0.6
0.2
-0.2
-0.6
-1.0

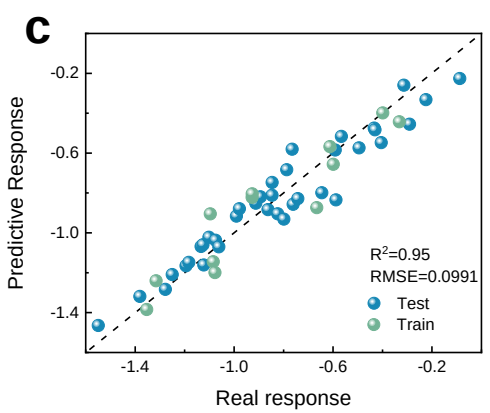
c
Predictive Response
Real response
-0.2
-0.6
-1.0
-1.4
R^2=0.95
RMSE=0.0991
Test
Train

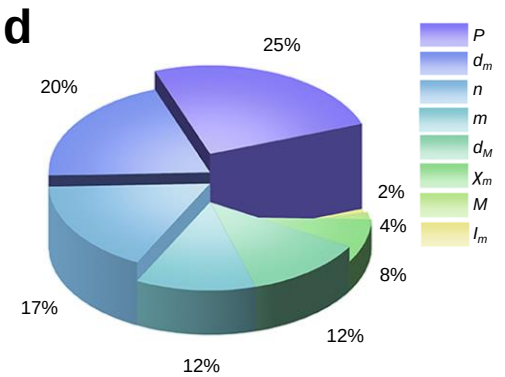
d
25%
20%
2%
4%
8%
17%
12%
12%
P
d_m
n
m
d_M
X_m
M
I_m

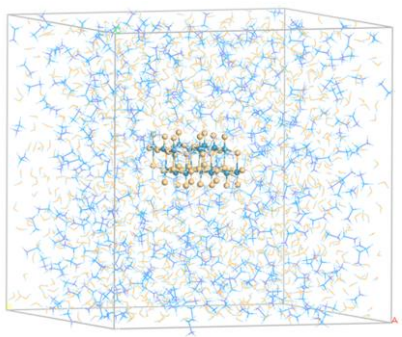
e

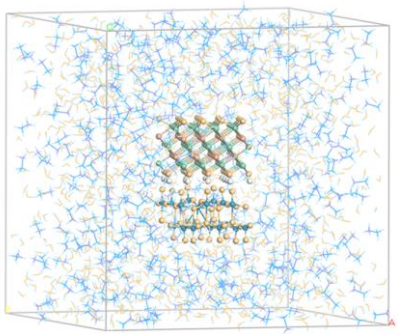
f

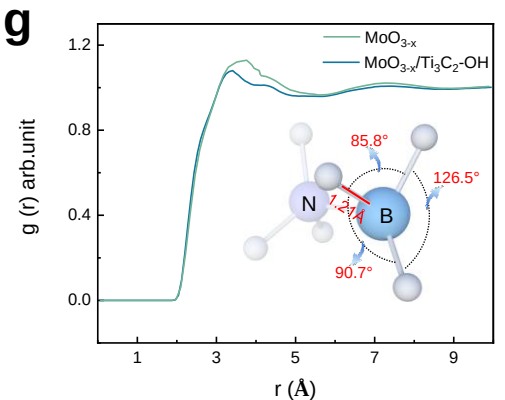
g
MoO_{3-x}
MoO_{3-x}/Ti_3C_2-OH
g (r) arb.unit
r (Å)
1.2
0.8
0.4
0.0
1
3
5
7
9
85.8°
126.5°
90.7°
N
B
1.27 Å

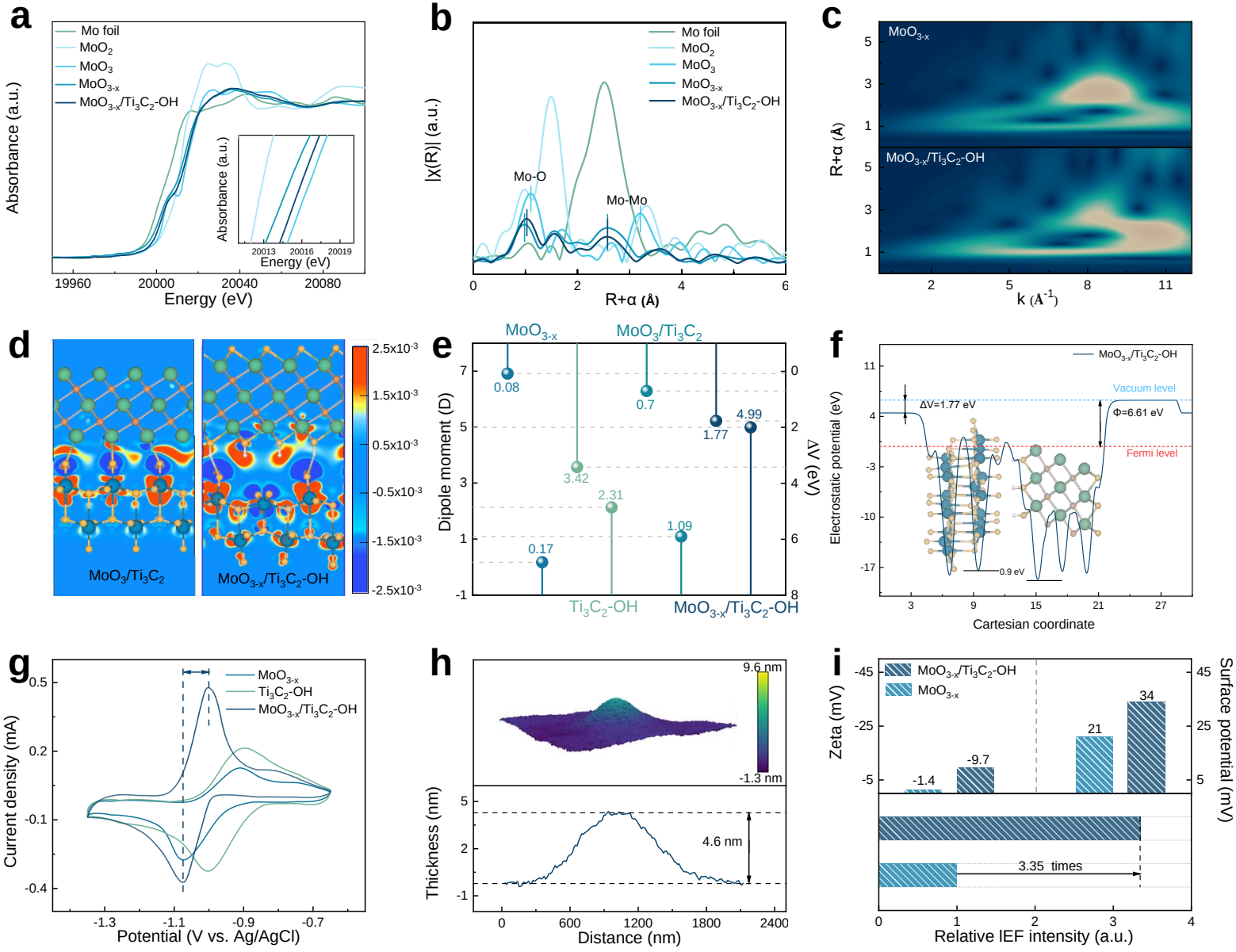
a
Mo foil
MoO2
MoO3
MoO3-x
MoO3-x/Ti3C2-OH
Absorbance (a.u.)
Energy (eV)
b
|χ(R)| (a.u.)
Mo-O
Mo-Mo
R+α (Å)
c
MoO3-x
MoO3-x/Ti3C2-OH
R+α (Å)
k (Å-1)
d
MoO3/Ti3C2
MoO3-x/Ti3C2-OH
e
MoO3-x
MoO3/Ti3C2
Dipole moment (D)
ΔV (eV)
Ti3C2-OH
MoO3-x/Ti3C2-OH
f
MoO3-x/Ti3C2-OH
Vacuum level
Fermi level
ΔV=1.77 eV
Φ=6.61 eV
Electrostatic potential (eV)
Cartesian coordinate
g
MoO3-x
Ti3C2-OH
MoO3-x/Ti3C2-OH
Current density (mA)
Potential (V vs. Ag/AgCl)
h
9.6 nm
-1.3 nm
Thickness (nm)
4.6 nm
Distance (nm)
i
MoO3-x/Ti3C2-OH
MoO3-x
Zeta (mV)
Surface potential (mV)
3.35 times
Relative IEF intensity (a.u.)

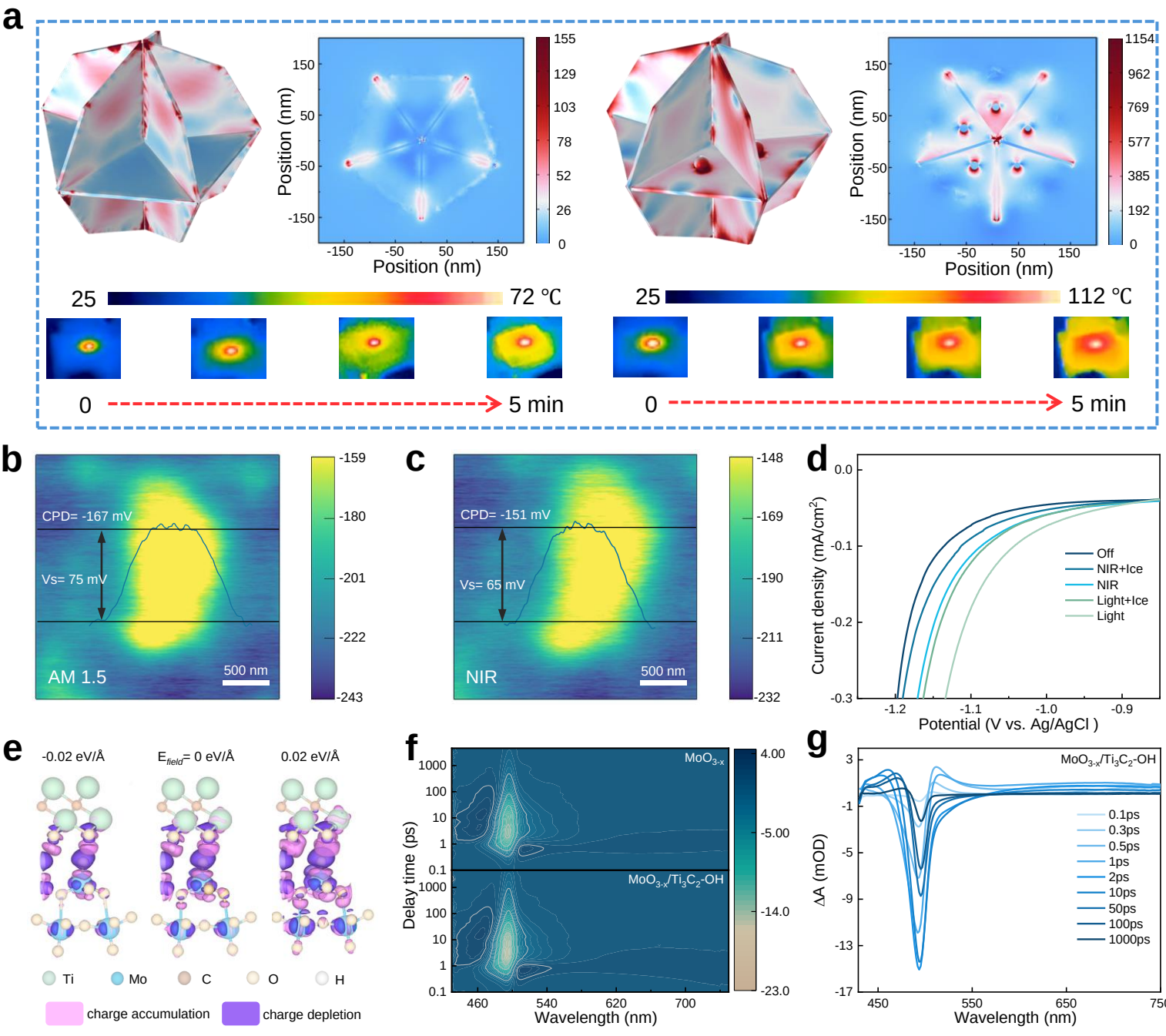
a
Position (nm)
155
129
103
78
52
26
0
1154
962
769
577
385
192
25
72 ℃
112 ℃
0
5 min
b
CPD= -167 mV
Vs= 75 mV
AM 1.5
500 nm
-159
-180
-201
-222
-243
c
CPD= -151 mV
Vs= 65 mV
NIR
500 nm
-148
-169
-190
-211
-232
d
Current density (mA/cm²)
Potential (V vs. Ag/AgCl)
Off
NIR+Ice
NIR
Light+Ice
Light
e
-0.02 eV/Å
E_field= 0 eV/Å
0.02 eV/Å
Ti
Mo
C
O
H
charge accumulation
charge depletion
f
MoO3-x
MoO3-x/Ti3C2-OH
Delay time (ps)
Wavelength (nm)
g
MoO3-x/Ti3C2-OH
ΔA (mOD)
0.1ps
0.3ps
0.5ps
1ps
2ps
10ps
50ps
100ps
1000ps
Wavelength (nm)

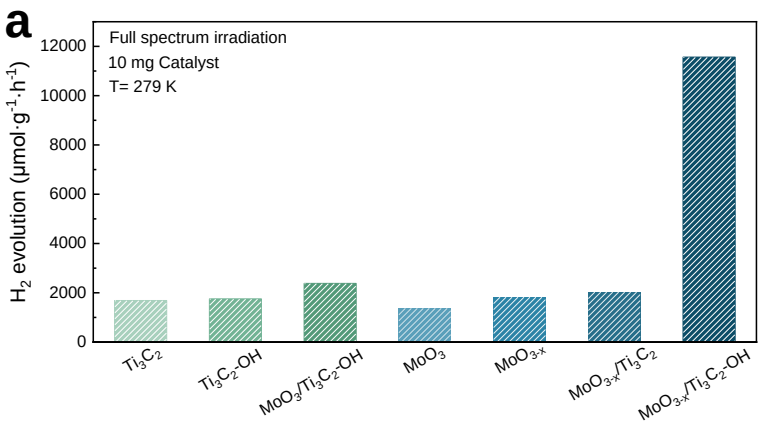
a
Full spectrum irradiation
10 mg Catalyst
T= 279 K
H2 evolution (μmol·g-1·h-1)
0
2000
4000
6000
8000
10000
12000
Ti3C2
Ti3C2-OH
MoO3/Ti3C2-OH
MoO3
MoO3-x
MoO3-x/Ti3C2
MoO3-x/Ti3C2-OH

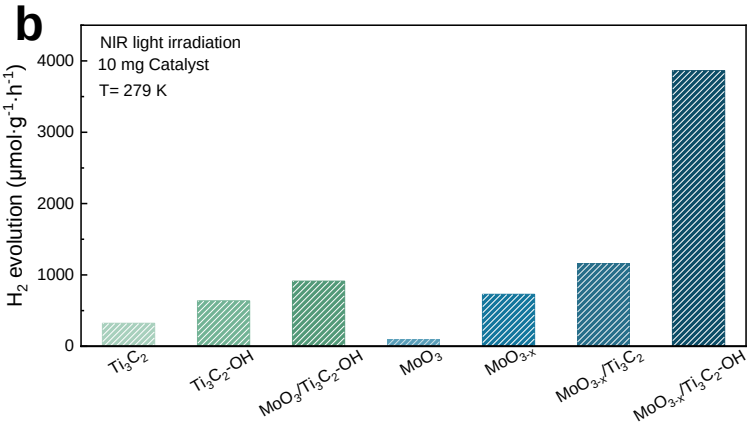
b
NIR light irradiation
10 mg Catalyst
T= 279 K
H2 evolution (μmol·g-1·h-1)
0
1000
2000
3000
4000
Ti3C2
Ti3C2-OH
MoO3/Ti3C2-OH
MoO3
MoO3-x
MoO3-x/Ti3C2
MoO3-x/Ti3C2-OH

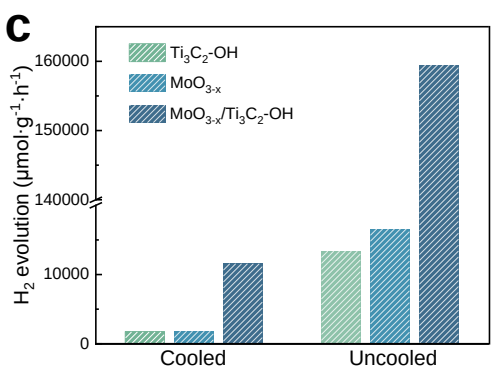
c
Ti3C2-OH
MoO3-x
MoO3-x/Ti3C2-OH
H2 evolution (μmol·g-1·h-1)
0
10000
140000
150000
160000
Cooled
Uncooled

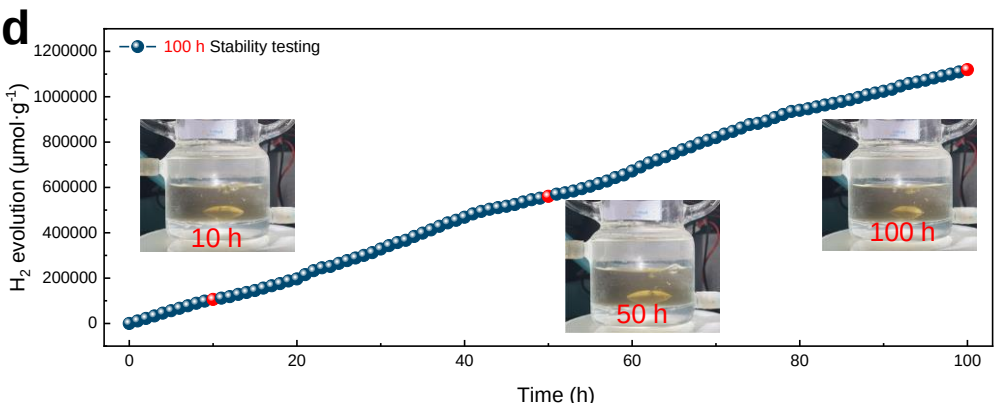
d
100 h Stability testing
H2 evolution (μmol·g-1)
0
200000
400000
600000
800000
1000000
1200000
10 h
50 h
100 h
0
20
40
60
80
100
Time (h)

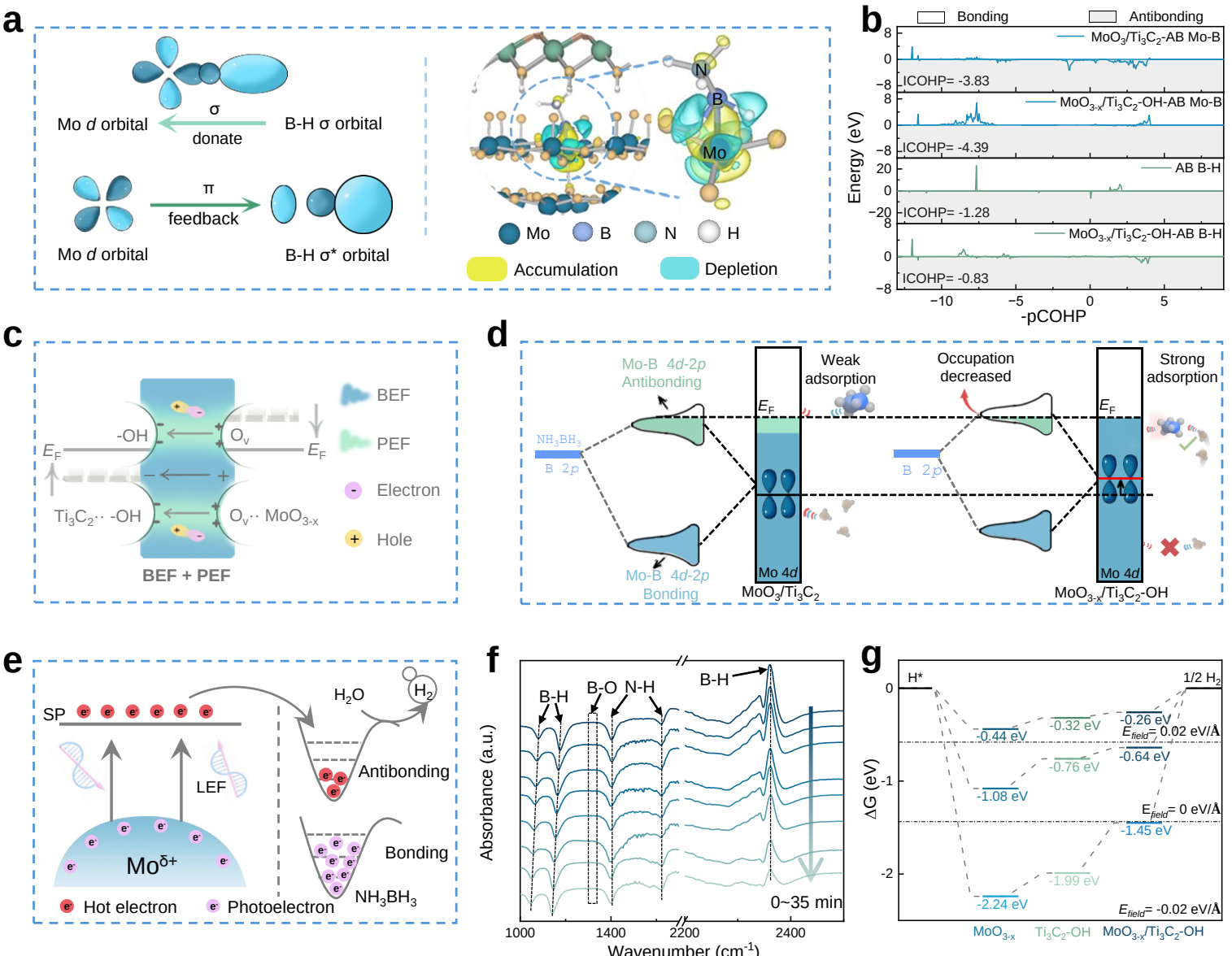
a
Mo d orbital
σ
donate
B-H σ orbital
π
feedback
Mo d orbital
B-H σ* orbital
N
B
Mo
Mo
B
N
H
Accumulation
Depletion
b
Bonding
Antibonding
MoO3/Ti3C2-AB Mo-B
ICOHP= -3.83
MoO3-x/Ti3C2-OH-AB Mo-B
ICOHP= -4.39
AB B-H
ICOHP= -1.28
MoO3-x/Ti3C2-OH-AB B-H
ICOHP= -0.83
Energy (eV)
-pCOHP
c
-OH
Ov
EF
EF
Ti3C2·· -OH
Ov·· MoO3-x
BEF
PEF
Electron
Hole
BEF + PEF
d
Mo-B 4d-2p
Antibonding
Weak
adsorption
Occupation
decreased
Strong
adsorption
NH3BH3
B 2p
EF
Mo 4d
Mo-B 4d-2p
Bonding
MoO3/Ti3C2
B 2p
EF
Mo 4d
MoO3-x/Ti3C2-OH
e
SP
LEF
Mo^δ+
H2O
H2
Antibonding
Bonding
NH3BH3
Hot electron
Photoelectron
f
B-H
B-O
N-H
B-H
Absorbance (a.u.)
0~35 min
Wavenumber (cm-1)
g
H*
1/2 H2
-0.44 eV
-0.32 eV
-0.26 eV
Efield= 0.02 eV/Å
-0.64 eV
-0.76 eV
-1.08 eV
Efield= 0 eV/Å
-1.45 eV
-1.99 eV
-2.24 eV
Efield= -0.02 eV/Å
ΔG (eV)
MoO3-x
Ti3C2-OH
MoO3-x/Ti3C2-OH